Bilinear noise subtraction at the GEO 600 observatory

N. Mukund,[1, a] J. Lough,[1] C. Affeldt,[1] F. Bergamin,[1] A. Bisht,[1] M. Brinkmann,[1] V. Kringel,[1] H. Lück,[1] S. Nadji,[1] and M. Weinert[1]

[1] *Albert Einstein Institute, Hannover, Germany*

(Dated: January 3, 2020)

We develop a scheme to subtract off bilinear noise from the gravitational wave strain data and demonstrate it at the GEO 600 observatory. Modulations caused by test mass misalignments on longitudinal control signals are observed to have a broadband effect on the mid-frequency detector sensitivity ranging from 50 Hz to 500 Hz. We estimate this bilinear coupling by making use of narrow-band signal injections that are already in place for noise projection purposes. A coherent bilinear signal is constructed by a two-stage system identification process where the involved couplings are approximated in terms of stable rational functions. The time-domain filtering efficiency is observed to depend upon the system identification process especially when the involved transfer functions cover a large dynamic range and have multiple resonant features. We improve upon the existing filter design techniques by employing a Bayesian adaptive directed search strategy that optimizes across the several key parameters that affect the accuracy of the estimated model. The resulting post-offline subtraction leads to a suppression of modulation side-bands around the calibration lines along with a broadband reduction of the mid-frequency noise floor. The filter coefficients are updated periodically to account for any non-stationarities that can arise within the coupling. The observed increase in the astrophysical range and a reduction in the occurrence of non-astrophysical transients suggest that the above method is a viable data cleaning technique for current and future gravitational wave observatories.

I. INTRODUCTION

GEO 600 is a British-German gravitational wave detector [1, 2] located in Ruthe, Hannover that searches for signals in the audio-band frequencies generated from astrophysical sources such as black holes and neutron stars. It is a dual recycled Michelson laser interferometer[3, 4] with 600m long folded arms reaching an average peak sensitivity of 2×10^{-22} Hz$^{-1/2}$ at 1 kHz and works in tandem with the global network of detectors that includes Advanced LIGO and Advanced Virgo. GEO 600 pioneered the use of several key technologies [5] which subsequently were incorporated in the larger detectors. These include the use of a squeezed light source[6], monolithic suspension, signal recycling, active thermal compensation, and electrostatic drive-based actuation. Demonstration of consistent levels of squeezing over a year-long timescale[7] in particular has lead to a decrease in the shot noise limited noise floor by a factor close to 2. Over the last several years, the automated alignment and locking scheme has lead to the stable operation of the detector with a duty cycle which has consistently been above 80%. The data from the detector was utilized in constraining the properties of the probable post-merger signal from the low mass compact binary inspiral signal GW170817 [8]. More recent work [9] has also pointed out the relatively higher sensitivity of GEO 600 compared to other detectors in searches looking for dark matter field oscillations in the range 100 Hz to 10 kHz. This is primarily due to the absence of arm cavities at GEO 600 which results in higher laser power at the beam splitter thus enhancing the detectability of these elusive signals.

Similar to other GW detectors, the sensitivity of the instrument is affected both by fundamental noise sources arising from thermal, seismic or quantum mechanical properties of light and by technical ones arising from the various auxiliary control loops that are used to keep it in a stable operating point. The common strategy adopted, principally for seismic and technical noise sources, is to estimate the linear part of the coupling and subtract it off via online feedforward cancellation [10–13]. Since the strain and auxiliary channel data is saved to disk, it is also possible to perform offline subtraction at a later time. Such offline cleaning has the advantage that the original data is preserved and the appropriate filters can be re-estimated for every data segment thus minimizing the possibility of noise injection. Solutions based on Wiener filtering are effective in regressing environmental disturbances [14] and have been applied to tackle correlated magnetic noises arising from Schumman resonances [15] as well as gravity gradients caused by seismic surface waves [16–19]. Effectiveness of offline analysis was recently demonstrated in Advanced LIGO second observation run (O2) data where the removal of laser jitter coupling led to an improvement in the range sensitivity by a factor of 15% [20].

There have been a couple of works in the past that looked at effects from higher-order couplings on the searches for short duration transients. One such work [21] looked for statistically significant temporal coincidences between the GW strain channel and bilinear auxiliary channel combinations and used it to veto time segments thus decreasing the number of false triggers. When no prior information is available on the non-linear nature in

[a] nikhil.mukund@aei.mpg.de

which various signals are getting combined, higher-order statistics based quantities like quadratic phase coupling have been suggested [22] as an effective metric to identify the involved pair, e.g., such as the signals from slowly changing angular degrees of freedom of the various suspended optics and the fast varying ones controlling the length of various optical cavities.

In this work, we look into a form of bilinear coupling, arising from the longitudinal control of the signal recycling mirror and show how accurate system identification can help in time domain subtraction of these from the calibrated strain data. The main motivation towards this work arose mostly from the observation of significant sidebands around some of the narrow-band signal injections that are used to estimate the noise contributions arising from various degrees of freedom. Our motivation also stems from the observation of the mid-frequency (50 - 500 Hz) noise at GEO 600 which is observed to go up with the increase of input laser power. Past attempts to identify the source of this noise ruled out linear couplings and consequently pointed towards effects from higher-order couplings.

In section II we present the longitudinal control scheme and our knowledge about the coupling mechanism, section III talks about challenges encountered in the accurate system identification and the methods adopted to overcome those issues, section IV presents the post-subtraction results and talks about the effect on certain data quality metrics such as glitch rate, and improvements to the astrophysical range. Finally we present our conclusions in section V.

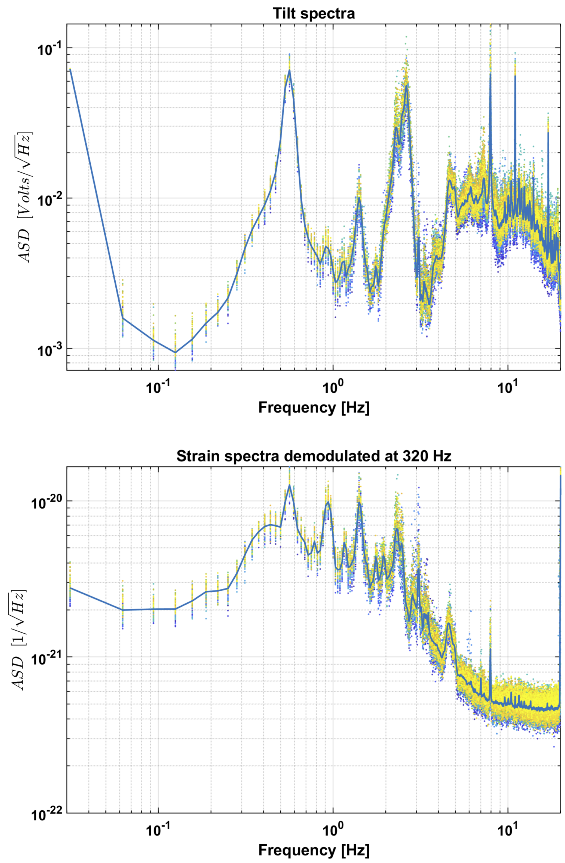

FIG. 2: Top plot shows spectra for differential tilt measured between end test mass mirrors and bottom one shows the GW strain signal demodulated at signal-recycling calibration line at 320 Hz. Each of the dotted line is constructed using 8 minute long segments and the solid line gives the median average for 12 hours of data.

II. COUPLING MECHANISM

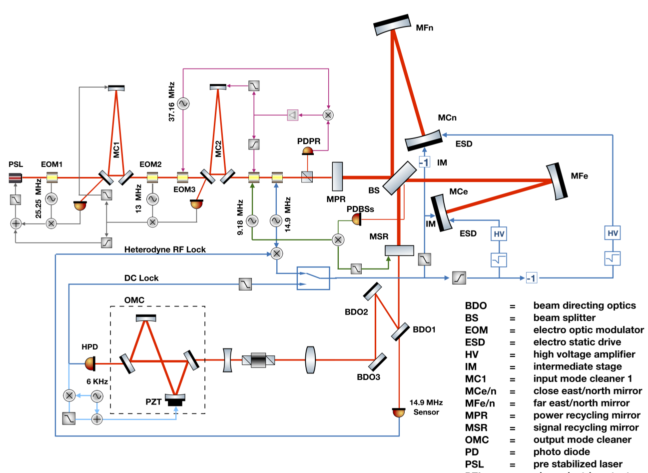

FIG. 1: Longitudinal control scheme of GEO 600 [23]

Dual recycling at GEO 600 consists of power recycling (PR) to increase the circulating carrier field and signal recycling (SR) to resonantly enhance the signal sidebands. Depending on the respective finesse of PR and SR cavities, this dual recycling enables the detector to have different storage time for carrier and storage signals. We can describe the frequency-dependent sensitivity of an interferometer in terms of the transfer function between the incident gravitational wave signal and the output photo-current at the photo-detector. For a dual recycled Michelson configuration, this response (normalized in terms of input power) is given as [24],

$$G(\omega) = \sqrt{\mathcal{G}_{arm}} \times \frac{-\tau_s}{1-\rho_s\rho_a e^{-i\omega t_r}} \times \frac{\rho_a\omega_0}{4}\frac{1-e^{-i\omega t_r}}{i\omega} \quad (1)$$

where $\mathcal{G}_{arm}$ is the ratio of power injected to that in the both arms; $\tau_s, \rho_s \& \rho_a$ are the respective transmittance and reflectivities of the mirrors that form the signal recycling cavity; ω_0 is the laser frequency, and t_r is the retarded time that incorporates the multiple reflections within the arm. To keep the detector in stable operating point and to maintain resonance in cavities it is necessary to keep the longitudinal motion of the key optics

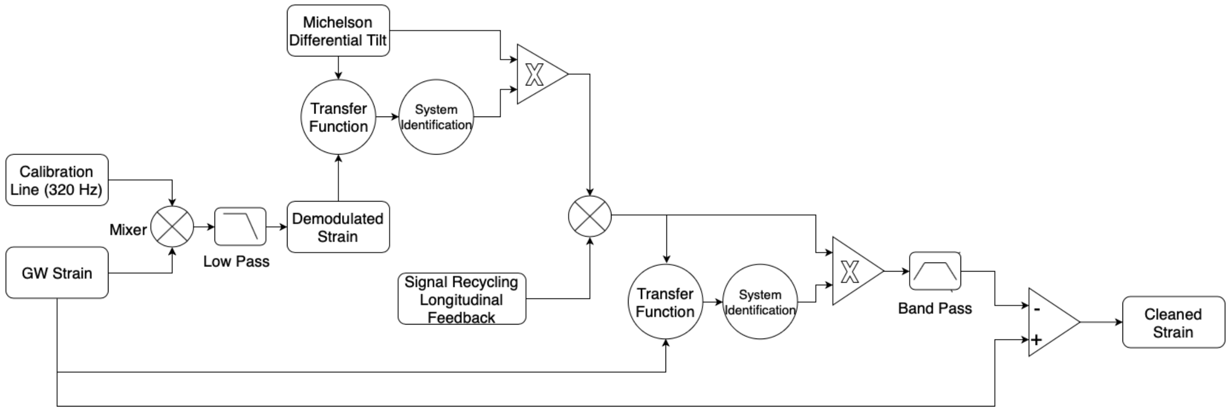

FIG. 3: Flow-graph depicting the steps involved in construction of a coherent bilinear signal from auxiliary channels.

limited to a fraction of the carrier field wavelength. This is achieved via multiple servo loops of which three are used for controlling the Michelson differential arm length as well as the length of PR and SR cavities. The scheme for the longitudinal control implemented at GEO 600 is depicted in Figure 1. The interferometer calibration process [25, 26] involved in the construction of the strain signal $(1/\sqrt(Hz))$ from the voltage fluctuations $(V/\sqrt(Hz))$ measured at the photodiode (labelled as HPD in Fig. 1), is usually done through the injection of known length modulations at specific frequencies. Such narrow-band lines are also often added to various control signals to get an estimate of their linear contributions to the GW sensitive signal. Specifically for the case of SR cavity length (SRCL) control, the addition happens digitally to the feedback signals before them being sent to the coil-magnet actuators. The SR mirror, in particular, is suspended via three-stage pendulum to damp the horizontal motion and two vertical cantilever spring stages to suppress the vertical disturbances. The longitudinal Pound-Hall-Drever (PDH) error signal is created by demodulating the light picked off from the anti-reflection coated side of the beam-splitter at Schnupp modulation side-band frequency, $f_{SR} = 9.18$ MHz. Actuation is carried out through a separate reaction chain using three magnet-coil actuators situated at its lowest stage. The SRCL control loop has a bandwidth of 35 Hz and linear coupling from this signal is one among the several technical noises that limit sensitivity at lower frequencies. The servo loop shape is observed to be dependant on factors such as the alignment, circulating power, time, etc and is the strongest known noise source up to 200 Hz [27]. The SRCL noise coupling to Michelson differential arises majorly from the small offset introduced between the end mirrors (2.0984×10^{-10} m) which leaks out a tiny amount of carrier light to the dark port to function as a local oscillator for the DC readout scheme [28, 29]. Efforts to suppress the out-of-bandwidth noise by making the controller transfer function roll-off steeper via low pass filtering is usually seen to add additional complexity as well as increased instability. Residual angular motion on any of the suspended optics can affect the circulating carrier field causing phase modulations and can ultimately show up in the strain data as a higher-order coupling. In particular, for GEO 600, the slight offset between the point of suspension and the horizontal axis of the test mass mirrors results in an enhanced length to angle coupling along with the tilt as compared to the rotational degree of freedom. Often, one of the first signs for such a coupling is the presence of sidebands seen around the injected line frequencies. Strain demodulated at the calibration line frequency shows multiple peaks with a structure similar to resonant modes of the test mass suspensions as shown in Figure 2. A high degree of coherence observed with the differential tilt further strengthens this possibility. In reality, angular motion is imprinted in the strain signal in a broadband sense but we prominently witness it around the calibration line because of its higher signal to noise ratio (SNR). These sidebands often vary in strength on time scales of few tens of minutes and could possibly have an effect on the transient noise level.

Non-Gaussian transients or glitches of instrumental origin and environmental disturbances increase the non-stationary nature of the data often leading to false triggers in template-based and un-modeled burst search pipelines that look for a true astrophysical signal. Advanced GW detectors apply different kinds of veto techniques to identify these events and minimize the false alarms[30]. Vetoes could be based on statistically significant temporal co-incidences between the strain and auxiliary data channels [31] or based on events seen in null-stream constructed out of the two calibrated strain quadratures [32]. For template-based searches, χ^2 time-frequency discriminator is often used to check for consistency between the trigger and expected event [33]. More recently techniques based on unsupervised and supervised learning have also been successful in identifying several glitch class populations observed in the strain data [34–37]. As compared to transient sources, the sensitiv-

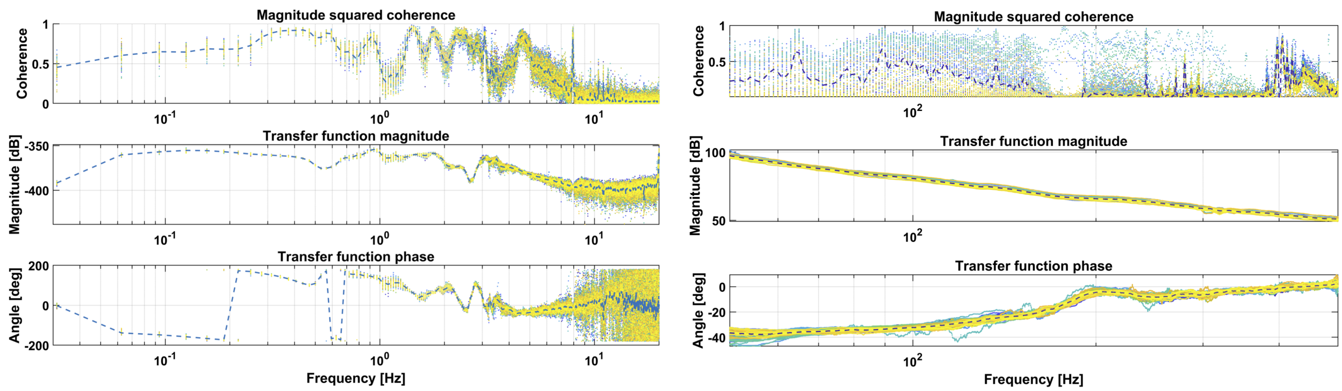

FIG. 4: Estimated transfer functions and their temporal variability. First plot models the coupling between differential tilt and demodulated strain while the second one provides the coupling between the constructed bilinear signal and measured strain signal. The dashed line gives the median average.

ity of GW searches looking for continuous wave signals is much more affected by persistent narrow-band spectral line features from power line harmonics or calibration lines. They require longer stretches of data that are often spread across multiple observation periods and so to minimize the contamination, a certain bandwidth (a few Hz) of data around these lines are often removed prior to carrying out the actual analysis. Constructing a coherent bilinear signal based on our understanding of the involved coupling, and carrying out a post-offline subtraction as described in the following section could thus lead to a certain degree of improvements in various data analysis pipelines.

III. SYSTEM IDENTIFICATION

Before the subtraction of nonlinear effects, it is necessary to ensure that the linear coupling is minimized. It stems from the de-tuning of the SR mirror and can be identified from the strain spectra as a more prominent central peak as compared to the sidebands. We carry out this length offset correction by feeding back the signal derived from the demodulating strain signal at one of the calibration line frequencies.

The procedure adopted for bilinear noise subtraction is depicted in Figure 3. It essentially involves two stages of linear system identification. To start with, we demodulate the strain signal at one of those frequencies where the SR calibration line is already and observe the linear contributions to it from various sensors that measure the angular motion of the various suspended optics. Of these, the witness channel that measures the differential tilt motion of the test mass mirrors provides the maximum coherence and is hence selected for further analysis. We estimate its transfer function to the demodulated strain, model it using an IIR filter and then extract the corresponding linear contribution. The desired bilinear signal is then constructed by taking the product of the filtered signal mentioned above and the feedback signal used for the longitudinal control of the SR mirror.

We make use of frequency-domain Bode diagrams to identify the linear coupling as these plots quickly reveal the dynamic range and sharp resonances involved within the coupling. As the optimal frequency resolution needed for the fast Fourier transform in the band of interest is not known apriori, we scan across a range of resolutions and choose the one which minimizes the phase jitter across the band of interest. We make use of the integral of the absolute value of the phase derivative across the mid-frequencies as the scalar metric to quantify this jitter. This transfer function is then modeled as an IIR filter, primarily so that our digital control system can keep up and also since it usually provides a better fit with a fewer number of filter coefficients as compared to an equivalent FIR representation. Updating the filter coefficients to tackle the non-stationaries has recently been shown to provide better subtraction for the case of non-linear noise observed in the LIGO detectors [38]. While analyzing the data spread across a period of 12 hours at GEO 600, we do observe slight variations in identified transfer functions as seen in Fig. 4.

Optimal modeling of the estimated transfer function is critical as any mis-representations can possibly lead to noise injection. Identifying complex zeros and poles to match the desired response especially in presence of noise can be considered as non-convex optimization problem. We express the unknown ZPK model as a rational function,

$$H(s) \approx \sum_{n=1}^{N} \frac{c_n}{s - a_n} + d + sh \ , \tag{2}$$

where c_n and a_n can either be real quantities or complex conjugate pairs, while d and h are both real. As the unknown poles a_n occur in the denominator, Eq. 2 cannot be directly solved as a linear problem. Using an unknown function $\sigma(s)$ and with an initial set of poles $\tilde{a}_n$ and zeros $\tilde{c}_n$, the above problem can be transformed into a linear

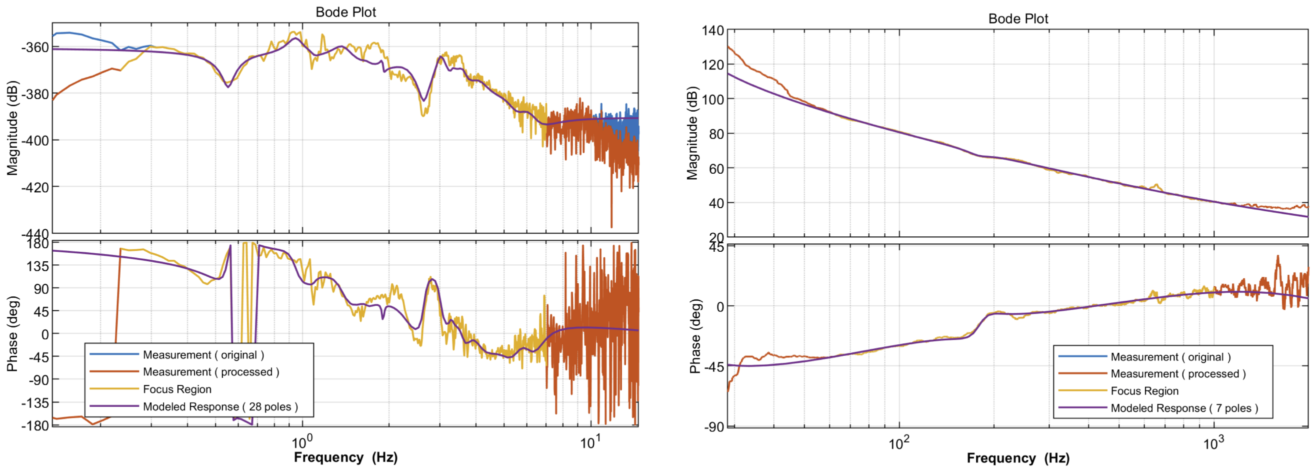

FIG. 5: System identification using bayesian adaptive directed search assisted vector fitting.

one,

$$\left(\sum_{n=1}^{N}\frac{c_n}{s-\tilde{a}_n}+d+sh\right)-\left(\sum_{n=1}^{N}\frac{\tilde{c}_n}{s-\tilde{a}_n}\right)H(s)\approx H(s)\ , \tag{3}$$

where

$$\begin{bmatrix}\sigma(s)H(s)\\ \sigma(s)\end{bmatrix}\approx\begin{bmatrix}\sum\limits_{n=1}^{N}\frac{c_n}{s-\tilde{a}_n}+d+sh\\ \sum\limits_{n=1}^{N}\frac{\tilde{c}_n}{s-\tilde{a}_n}+1\end{bmatrix}\ . \tag{4}$$

We then make use of Vector Fitting (VF) [39, 40] scheme to hierarchically solve the above equation in an iterative manner by first carrying out pole identification followed by the identification of residues, c_n. To obtain a better fit without suffering from issues related to ill-conditioning, we follow the typical strategy of starting with complex conjugate pole pairs whose imaginary part spans either linearly or logarithmically the frequency span of interest. The routine further enforces stability by forcing all the poles to be on the left half-plane in the continuous Laplace domain. The quality of the fit is assessed using normalized root mean square error metric,

$$nrmse(y)=\frac{\|y-\hat{y}\|}{\|y-mean(y)\|}\ , \tag{5}$$

where y and $\hat{y}$ respectively are the measured and modeled response.

The initial pole placement, number of poles, frequency-dependent weighting factor, initial and final frequencies are unknown factors whose value affects the overall quality of the fitted model. To optimize across these, we make use of Bayesian Adaptive Directed Search (BADS) [41] to search across the respective parameter space without much invoking a heavy computational overhead. Bayesian Optimization (BO) is typically used in machine learning applications for model fitting especially when the cost functions are expensive to calculate such as those encountered in hyper-parameter tuning but usually comes with large algorithmic overhead and requires some amount of fine-tuning. The advantage of BADS comes from its use of derivative-free mesh adaptive direct search combined with its use of BO via surrogates based on the Gaussian process which drastically speeds up the function evaluations. Using the above-mentioned procedure, we obtain a reasonably good fit for the estimated transfer functions as shown in Figure 5. Before performing time-domain filtering, we discretize the continuous domain model at the sampling frequency (16 kHz) and then finally converted it to second-order-sections to overcome the issues related to numerical rounding errors [42, 43].

Finally, to achieve optimal subtraction, we address the issue related to the presence of non-stationarities in each of the identified couplings. Often as a result of ongoing commissioning activities at the site, the intermediate filters in the actuation path are very likely to get modified hence re-calculating the filter coefficients is, in general, a desirable strategy. We carry out periodic system identification for every eight minutes long data stretch and accordingly subtract the bilinear component from the strain data.

IV. RESULTS

In this analysis, we made use of half a day of data recorded during the first observation run period of Advanced LIGO (O1). This period was specifically chosen as it had the highest contamination from the above described bilinear coupling. In Figure 6, we show the estimated bilinear noise contribution from SR longitudinal to the strain signal for a typical hour-long data and provide the cleaned signal after carrying out time-domain subtraction. Figure 7 provides the average levels of subtraction achieved across the mid-frequencies for the entire duration of the data. In general, we see a broadband

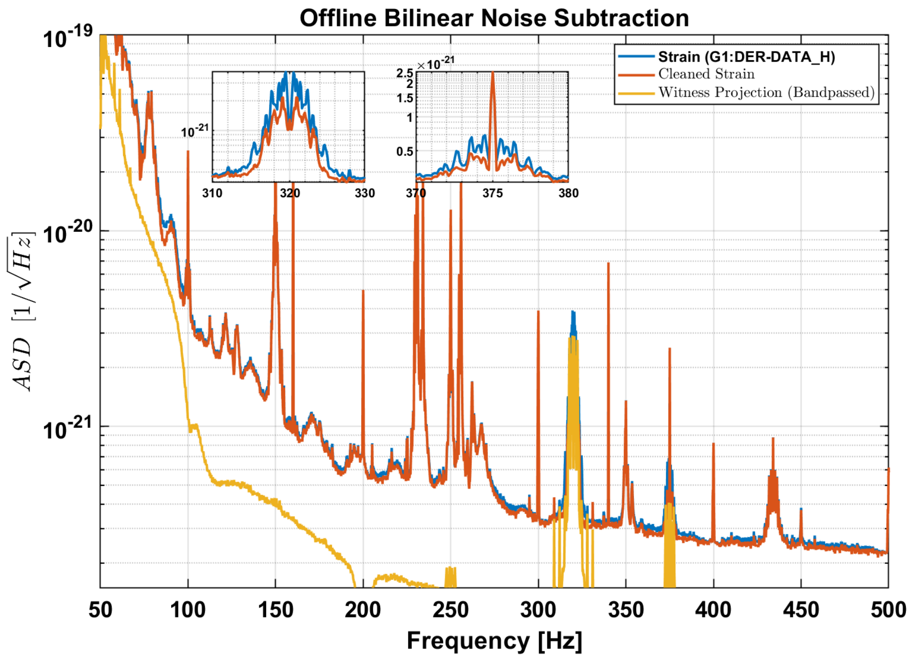

FIG. 6: Broadband Improvements to GEO 600 strain sensitivity after bilinear noise subtraction. Plots are constructed using 3600 seconds data starting from 21-09-2015 23:00:00 (UTC). Inset plots show sideband suppression around calibration lines at 320 Hz and 375 Hz.

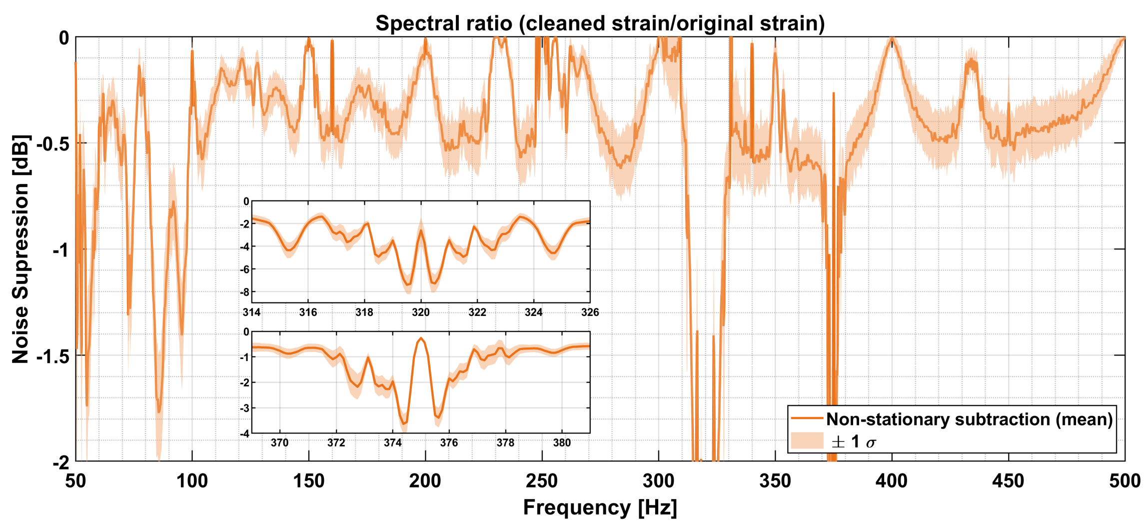

FIG. 7: Broadband Improvements to GEO 600 strain sensitivity after bilinear noise subtraction. Plots are constructed using 3600 seconds data starting from 21-09-2015 23:00:00 (UTC). Inset plots show sideband suppression around calibration lines at 320 Hz and 375 Hz.

reduction in the noise levels, where the level of suppression is determined by the coherence between strain and the constructed bilinear signal. Maximum suppression is achieved for the sidebands seen around 320 Hz (∼8 dB) and 375 Hz (∼4 dB). The calibration line at 375 Hz is injected via the power recycling mirror, hence the fact that we are able to subtract off its side-bands using SR feedback indicates a cross-coupling between PR and SR cavities.

Since improvement to the astrophysical range is a use-

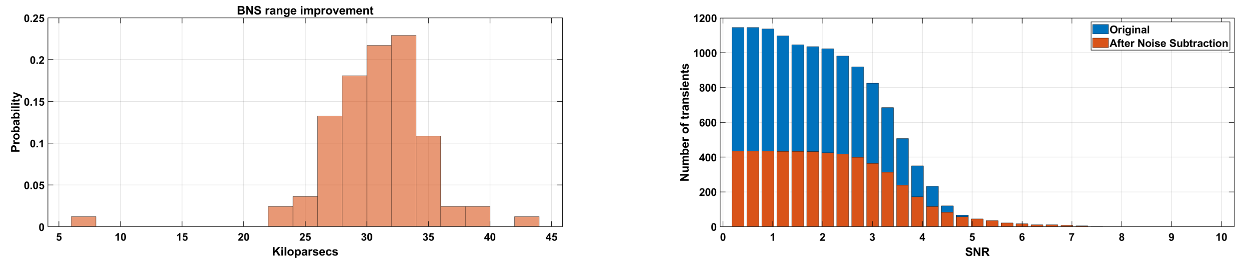

FIG. 8: Improvements in data quality. The first plot shows the increase in horizon distance for an optimally located and oriented binary neutron star of 1.4 solar mass each. The second plot gives the cumulative histogram of excess power transients above a given SNR before and after the bilinear noise subtraction.

ful data quality metric, we look at the horizon distance [44, 45] for an optimally located and oriented binary neutron star of 1.4 solar mass each and obtain a modest improvement of 30 kilo-parsecs (subplot 1 of Figure 8) over the baseline sensitivity of 2.49 Mpc (2015 O1 data). To assess the impact on transient searches, it is desirable to check the excess power events before and after the subtraction. As a pre-processing step towards this analysis, we first whiten the strain data to enhance the high-frequency content and then subject it to a multi-resolution analysis for every one-second-long data segment. Time-frequency scalograms are constructed via continuous wavelet transformation using analytic Morlet wavelet [46, 47] and the pixels with excess energy within them are identified using the Hierarchical Algorithm for Clusters and Ridges (HACR) algorithm [48]. Subplot 2 of Figure 8 shows the cumulative histogram of transients with SNR is less than a given threshold and the effectiveness of bilinear subtraction is visibly evident.

V. CONCLUSIONS

We presented a post-offline scheme to perform the time-domain subtraction of one form of bilinear coupling often observed in GW detectors and demonstrated it using the GEO 600 detector data. We made use of existing narrow-band injections to identify the coupling and showed that it is indeed possible to achieve suppression of side-bands as well as broadband noise reduction in the mid-frequency range. The analysis broadened our understanding of possible contributors to the non-stationary noise which is often encountered when the detector operates at higher levels of circulating power. Side-band suppression demonstrated in this work could be beneficial in the searches looking for continuous waves, but further analysis is needed to qualitatively analyze the impact. The observed glitch reduction implies such a scheme could be used in conjunction with traditional veto and gating based techniques to improve the significance of true events in transient searches. Although the technique presented in this work was applied to reduce the bilinear coupling, it could be extended further to tackle higher-order couplings present in the data. Developing automated techniques to identify and subtract them off in real-time would be part of future work.

VI. ACKNOWLEDGMENTS.

We thank the GEO collaboration for the construction of GEO 600; Walter Graß for his work in keeping the interferometer in a good running state. NM expresses thanks to Denis Martynov and Gautam Venugopalan for their valuable comments and suggestions. Authors are grateful for support from the Science and Technology Facilities Council (STFC) Grant Ref: ST/L000946/1, the University of Glasgow in the UK, the Bundesministerium für Bildung und Forschung (BMBF), and the state of Lower Saxony in Germany. This work was partly supported by DFG grant SFB/Transregio 7 Gravitational Wave Astronomy. This document has been assigned LIGO document number LIGO-P1900350.

[1] B. Willke *et al.*, Classical and Quantum Gravity **19**, 1377 (2002).
[2] H. Lück et al., Class. Quantum Grav. **23**, S71 (2006).
[3] H. Lück, C. Affeldt, J. Degallaix, A. Freise, H. Grote, M. Hewitson, S. Hild, J. Leong, M. Prijatelj, K. A. Strain, B. Willke, H. Wittel, and K. Danzmann, J. Phys.: Conf. Series **228**, 012012 (2010).
[4] K. L. Dooley, J. R. Leong, T. Adams, *et al.*, Classical and Quantum Gravity **33**, 075009 (2016).
[5] C. Affeldt, K. Danzmann, K. Dooley, H. Grote, M. Hewitson, S. Hild, J. Hough, J. Leong, H. Lück, M. Prijatelj, *et al.*, Classical and quantum gravity **31**, 224002 (2014).
[6] J. Abadie, B. P. Abbott, R. Abbott, T. D. Abbott, M. Abernathy, C. Adams, R. Adhikari, C. Affeldt, B. Allen, G. Allen, *et al.*, Nature Physics **7**, 962 (2011).

[7] H. Grote, K. Danzmann, K. Dooley, R. Schnabel, J. Slutsky, and H. Vahlbruch, Physical review letters **110**, 181101 (2013).

[8] B. P. Abbott *et al.* (LIGO Scientific Collaboration and Virgo Collaboration), Phys. Rev. X **9**, 011001 (2019).

[9] H. Grote and Y. Stadnik, arXiv preprint arXiv:1906.06193 (2019).

[10] J. A. Giaime, E. J. Daw, M. Weitz, R. Adhikari, P. Fritschel, R. Abbott, R. Bork, and J. Heefner, Rev. Sci. Instrum. **74**, 218 (2003).

[11] J. Smith, H. Grote, M. Hewitson, S. Hild, H. Lück, M. Parsons, K. A. Strain, and B. Willke, Classical and Quantum Gravity **22**, 3093 (2005).

[12] J. C. Driggers, M. Evans, K. Pepper, and R. Adhikari, Rev. Sci. Instrum. **83**, 024501 (2012), arXiv:1112.2224 [gr-qc].

[13] G. D. Meadors, K. Kawabe, and K. Riles, Class. Quant. Grav. **31**, 105014 (2014), arXiv:1311.6835 [astro-ph.IM].

[14] V. Tiwari, M. Drago, V. Frolov, S. Klimenko, G. Mitselmakher, V. Necula, G. Prodi, V. Re, F. Salemi, G. Vedovato, and I. Yakushin, Classical and Quantum Gravity **32**, 165014 (2015).

[15] M. W. Coughlin, A. Cirone, P. Meyers, S. Atsuta, V. Boschi, A. Chincarini, N. L. Christensen, R. De Rosa, A. Effler, I. Fiori, and et al., Physical Review D **97** (2018), 10.1103/physrevd.97.102007.

[16] G. Cella, in *Recent Developments in General Relativity*, edited by B. Casciaro, D. Fortunato, M. Francaviglia, and A. Masiello (Springer Milan, Milano, 2000) pp. 495–503.

[17] M. G. Beker, J. F. J. van den Brand, E. Hennes, and D. S. Rabeling, Journal of Physics: Conference Series **363**, 012004 (2012).

[18] J. C. Driggers, J. Harms, and R. X. Adhikari, Physical Review D **86** (2012), 10.1103/physrevd.86.102001.

[19] M. Coughlin, N. Mukund, J. Harms, J. Driggers, R. Adhikari, and S. Mitra, Classical and Quantum Gravity **33**, 244001 (2016).

[20] J. C. Driggers *et al.* (The LIGO Scientific Collaboration Instrument Science Authors), Phys. Rev. D **99**, 042001 (2019).

[21] P. Ajith, T. Isogai, N. Christensen, R. X. Adhikari, A. B. Pearlman, A. Wein, A. J. Weinstein, and B. Yuan, Phys. Rev. D **89**, 122001 (2014).

[22] S. Bose, B. Hall, N. Mazumder, S. Dhurandhar, A. Gupta, and A. Lundgren, *Proceedings, 11th Edoardo Amaldi Conference on Gravitational Waves (Amaldi 11): Gwangju, South Korea, June 21-26, 2015*, J. Phys. Conf. Ser. **716**, 012007 (2016), arXiv:1602.02621 [astro-ph.IM].

[23] H. Grote, *Making it Work: Second Generation Interferometry in GEO600!*, Ph.D. thesis, Universität Hannover Hannover (2003).

[24] J. Mizuno, *Comparison of optical configurations for laser-interferometric gravitational-wave detectors*, Ph.D. thesis, AEI-Hannover, MPI for Gravitational Physics, Max Planck Society (1995).

[25] M. Hewitson, H. Grote, G. Heinzel, K. A. Strain, H. Ward, and U. Weiland, Classical and Quantum Gravity **20**, S885 (2003).

[26] J. R. Leong, M. Hewitson, H. LÃijck, H. Grote, S. Hild, C. Affeldt, J. Degallaix, A. Freise, M. Prijatelj, K. Strain, H. Wittel, B. Willke, and K. Danzmann, Classical and Quantum Gravity **29**, 065001 (2012).

[27] H. Wittel, LIGO DCC **G1700418** (2017).

[28] K. Izumi and D. Sigg, Classical and Quantum Gravity **34**, 015001 (2016).

[29] V. B. Adya, *Ways to stop mirrors from moving unnecessarily: design of advanced gravitational wave detectors*, Ph.D. thesis, Universität Hannover Hannover (2018).

[30] J. Slutsky, L. Blackburn, D. Brown, L. Cadonati, J. Cain, M. Cavaglia, S. Chatterji, N. Christensen, M. Coughlin, S. Desai, *et al.*, Classical and Quantum Gravity **27**, 165023 (2010).

[31] J. R. Smith, T. Abbott, E. Hirose, N. Leroy, D. MacLeod, J. McIver, P. Saulson, and P. Shawhan, Classical and Quantum Gravity **28**, 235005 (2011).

[32] M. Hewitson and P. Ajith, Classical and Quantum Gravity **22**, 4903 (2005).

[33] B. Allen, Phys. Rev. D **71**, 062001 (2005).

[34] R. Biswas *et al.*, Phys. Rev. D **88**, 062003 (2013).

[35] J. Powell, D. Trifirò, E. Cuoco, I. S. Heng, and M. Cavaglià, Classical Quantum Gravity **32**, 215012 (2015).

[36] N. Mukund, S. Abraham, S. Kandhasamy, S. Mitra, and N. S. Philip, Phys. Rev. D **95**, 104059 (2017).

[37] M. Zevin, S. Coughlin, S. Bahaadini, E. Besler, N. Rohani, S. Allen, M. Cabero, K. Crowston, A. K. Katsaggelos, S. L. Larson, T. K. Lee, C. Lintott, T. B. Littenberg, A. Lundgren, C. ÃŸsterlund, J. R. Smith, L. Trouille, and V. Kalogera, Classical Quantum Gravity **34**, 064003 (2017).

[38] G. Vajente, Y. Huang, M. Isi, J. C. Driggers, J. S. Kissel, M. J. Szczepanczyk, and S. Vitale, "Machine-learning non-stationary noise out of gravitational wave detectors," (2019), arXiv:1911.09083 [gr-qc].

[39] B. Gustavsen and A. Semlyen, IEEE Transactions on power delivery **14**, 1052 (1999).

[40] B. Gustavsen, in *Signal Propagation on Interconnects, 2006. IEEE Workshop on* (IEEE, 2006) pp. 97–100.

[41] L. Acerbi and W. Ji, in *Advances in neural information processing systems* (2017) pp. 1836–1846.

[42] S. K. Mitra and Y. Kuo, *Digital signal processing: a computer-based approach*, Vol. 2 (McGraw-Hill New York, 2006).

[43] L. B. Jackson, *Digital Filters and Signal Processing: With MATLAB® Exercises* (Springer Science & Business Media, 2013).

[44] L. S. Finn and D. F. Chernoff, Phys. Rev. D **47**, 2198 (1993).

[45] H.-Y. Chen, D. E. Holz, J. Miller, M. Evans, S. Vitale, and J. Creighton, arXiv preprint arXiv:1709.08079 (2017).

[46] S. Mallat, *A wavelet tour of signal processing* (Elsevier, 1999).

[47] J. M. Lilly and S. C. Olhede, IEEE Transactions on Signal Processing **60**, 6036 (2012).

[48] I. S. Heng, R. Balasubramanian, B. S. Sathyaprakash, and B. F. Schutz, Classical and Quantum Gravity **21**, S821 (2004).